


Preferred location for conducting filament formation in thin-film nano-ionic electrolyte: study of microstructure by atom-probe tomography

Jiri Orava^{1,2}  · Yuren Wen³ · Jan Prikryl⁴ · Tomas Wagner^{4,5} ·
Nadia A. Stelmashenko¹ · Mingwei Chen² · A. Lindsay Greer^{1,2}

Received: 3 November 2016 / Accepted: 13 January 2017 / Published online: 2 February 2017
© The Author(s) 2017. This article is published with open access at Springerlink.com

Abstract Atom-probe tomography of Ag-photodoped amorphous thin-film $\text{Ge}_{40}\text{S}_{60}$, the material of interest in nano-ionic memory and lateral geometry MEMS technologies, reveals regions with two distinct compositions on a nanometer length-scale. One type of region is Ag-rich and of a size typically extending beyond the measured sample volume of $\sim 40 \times 40 \times 80 \text{ nm}^3$. These type-I regions contain aligned nanocolumns, $\sim 5 \text{ nm}$ wide, that are the likely location for reversible diffusion of Ag^+ ions and associated growth/dissolution of conducting filaments. The nanocolumns become relatively Ag-rich during the photodoping,

and the pattern of Ag enrichment originates from the columnar-porous structure of the as-deposited film that is to some extent preserved in the electrolyte after photodoping. Type-II regions have lower Ag content, are typically 10–20 nm across, and appear to conform to the usual description of the photoreaction products of the optically-induced dissolution and diffusion of silver in a thin-film chalcogenide. The microstructure, with two types of region and aligned nanocolumns, is present in the electrolyte after photodoping without any applied bias, and is important for understanding switching mechanisms, and writing and erasing cycles, in programmable-metallization-cell memory.

Electronic supplementary material The online version of this article (doi:[10.1007/s10854-017-6383-y](https://doi.org/10.1007/s10854-017-6383-y)) contains supplementary material, which is available to authorized users.

✉ Jiri Orava
jo316@cam.ac.uk

✉ A. Lindsay Greer
alg13@cam.ac.uk

¹ Department of Materials Science & Metallurgy, University of Cambridge, 27 Charles Babbage Road, Cambridge CB3 0FS, UK

² WPI-Advanced Institute for Materials Research (WPI-AIMR), Tohoku University, 2-1-1 Katahira, Aoba-ku, Sendai 980-8577, Japan

³ Beijing Laboratory for Electron Microscopy, Institute of Physics, Chinese Academy of Sciences, No. 8, 3rd South Street, Zhongguancun, Haidian District, Beijing 100190, China

⁴ Centre for Nanomaterials & Nanotechnology (CEMNAT), Faculty of Chemical Technology, University of Pardubice, Cs. Legii Sq. 565, 532 10 Pardubice, Czech Republic

⁵ Department of General & Inorganic Chemistry, Faculty of Chemical Technology, University of Pardubice, Studentska 95, 532 10 Pardubice, Czech Republic

1 Introduction

Amorphous chalcogenides (a-Chs), doped predominantly with Ag or Cu, have been widely studied because of their applications in nano-ionic devices such as *programmable-metallization-cell* (PMC) memory (also known as *conductive-bridging random-access memory* CB-RAM) [1–3], MEMS technology [4], photonic devices [5], inorganic resists [6] and ion-selective electrodes [7]. Electrically- and optically-induced fast diffusion of Ag^+ ions is the basis for on-demand physico-chemical changes (e.g. of resistance [3, 4], complex dielectric function [5], and chemical reaction mechanism [6]) in a-Ch solid-state electrolytes.

In PMC memory, Ag-photodoped a-Ge-S or a-Ge-Se is typically used as the active layer, in contact with a bottom inert (Pt, W, Au...) electrode and a top Ag electrode. Writing, leading to the low-resistance ON state, involves the growth of metallic silver conducting filaments, CFs. On applying a voltage with the bottom electrode acting as cathode and the top electrode as anode, the filaments

grow through the a-Ch thin film; in this case the Ag^+ ions migrate towards the cathode, enabling the metallic CF to grow from the cathode towards the anode. The CFs are estimated to be some tens of nanometers wide and are often in the form of a cone based on the cathode [2], unlike the dendritic shape observed for CF growth on samples with lateral geometry [8]. Erasing occurs by dissolution of the CF on reversing the polarity, leading to the high-resistance OFF state. This bi-polar switching is attractive for device applications as it takes less than 50 ns and requires an energy of only $\sim 10^{-15}$ J [9].

Among different doping techniques [10, 11], the focus here is on Ag photodoping. In making the active region in PMC memory, a thin film (~ 30 nm) of silver is deposited onto an a-Ch layer itself < 100 nm thick. This Ag/chalcogenide bi-layer is exposed to ultraviolet and white-light sources, exciting electron-hole pairs that, when they are formed near the Ag/a-Ch interface, enable *optically-induced dissolution and diffusion* (OIDD). Electrons are trapped at the chalcogen atom (C_2^0), $2\text{C}_2^0 \xrightarrow{h\nu} \text{C}_1^- + \text{C}_3^+$, creating over-coordinated C_3^+ , and under-coordinated C_1^- , structural defects (the superscript indicates the charge state and the subscript the coordination number). The holes can drift and ionize silver atoms, $\text{Ag} + h^+ \rightleftharpoons \text{Ag}^+$ [12]. In OIDD, the migration of Ag^+ ions is driven by the internal electric field. OIDD is directional: Ag^+ ions migrate in the direction of the actinic light, and sharp concentration edges are formed between exposed (Ag-photodoped) and unexposed (Ag-undoped) regions [13].

Conventionally, OIDD is assumed to involve formation of an amorphous metastable reaction layer at the Ag/a-Ch interface, giving a distinct diffusion front that migrates through the sample. The composition of the advancing photodoped region is close to AgAsS_2 in Ag-As-S glass [12]. In the initial stages of OIDD the silver concentration is non-uniform through the film thickness, but the concentration gradient decreases with increasing exposure time [14, 15]. OIDD gives a product that is spatially non-uniform in composition [16–19]. Ag-rich and Ag-poor regions are formed; this non-uniformity has been conventionally attributed to phase separation similar to that observed in glasses prepared by cooling a liquid. The chalcogenide electrolyte can be considered to be a fine-scale amorphous composite. The reaction products of OIDD are generally considered to remain non-crystalline, but nanocrystals of $\text{Ag}_2\text{S}(\text{Se})$ and $\text{Ag-Ge-S}(\text{Se})$, tens of nanometers in diameter, have been detected [18, 19].

When concerned with electrically-induced migration of Ag^+ ions, the structure and uniformity of the material are of direct interest. Switching in the memory electrolyte involves several processes: oxidation of the active electrode, Ag^+ migration, reduction at the electrolyte/inert

electrode interface, nucleation and CFs growth (dissolution on the bias reversal), and electron tunneling [20]. Whether the switching is limited by nucleation, by electron-transfer, or by mixed electron-transfer and ion hopping [20, 21], where one or more of these rate-limiting steps can be present, is strongly influenced by the electrolyte composition. Are conducting pathways already present in the material after OIDD, or do they form later as the result of the applied voltage? Pathways along which conduction is favored would certainly influence the growth and dissolution kinetics, also subjected to the stress field that develops [22], and the morphology and stability of CFs. But the role of non-uniformity in the a-Ch on the formation of CFs remains unknown. A major experimental difficulty is that the imaging technique itself can induce structural modifications and damage [23].

In this letter, *local-electrode atom-probe tomography* (LEAPT) is used to study the microstructure of Ag-photodoped thin-film $\text{Ge}_{40}\text{S}_{60}$ immediately after OIDD, in an attempt to identify possible preferred locations for the formation of CFs. For an actual material used in PMC memory, we provide the first report of direct observations of microstructure with nm resolution in 3-D (in contrast to earlier 2-D studies with μm resolution; see refs [24, 25] and the references therein).

2 Experimental methods

A 5 nm layer of Pt was sputtered at an argon pressure of ~ 3.4 Pa and at a power of 25 W onto a 6×6 array of pre-sharpened silicon tips (PSM M36 by CAMECA), each with radius of curvature < 50 nm; the silicon was heavily n-doped with a resistivity of $< 0.1 \Omega \text{ cm}$. Thin-film $\text{Ge}_{40}\text{S}_{60}$, ~ 80 nm thick, was deposited by flash evaporation [26] from a $\text{Ge}_{40}\text{S}_{60}$ target at an evaporation rate of $0.1\text{--}0.3 \text{ nm s}^{-1}$ under a residual pressure of $\sim 10^{-4}$ Pa. A silver layer, ~ 30 nm thick, was thermally evaporated on to the $\text{Ge}_{40}\text{S}_{60}$ at a rate of $\sim 0.1\text{--}0.2 \text{ nm s}^{-1}$ under a residual pressure of $\sim 10^{-4}$ Pa. A halogen lamp (150 W) was used to achieve the OIDD of Ag into the chalcogenide film under argon atmosphere. The photodoped samples were stored under dark conditions. Any remaining silver on top was not removed prior to the atom-probe experiments.

The composition of the films was verified by SEM combined with EDS (JEOL JIB-4600F) and the Ge:S ratio after the photodoping was found to be $0.68 (\pm 0.04)$. The accurate content of Ag could not be determined because of the e-beam induced migration; the overall content of Ag is above the percolation threshold for conductivity [27]. For the main study, a CAMECA LEAP 4000HR was used in a pulse-voltage mode, and the samples were cooled to 80 K during the measurement to prevent surface reconstruction.

Atom-probe data were processed and images reconstructed with CAMECA IVAS 3.6.6 software. In total, six samples were reproducibly reconstructed, all of them showing the same trends as presented in the text.

3 Results and discussion

Figure 1 shows a characteristic time-of-flight (TOF) mass spectrum obtained from a $\text{Ag-Ge}_{40}\text{S}_{60}$ sample during electric-field evaporation in the LEAPT chamber. The presence of the underlying cathode layer of Pt, the Si substrate, and the formation of GeO_x can be detected, but the TOF signal is dominated by monatomic Ag^+ and S^+ (with a few S_2^+) ions, with smaller peaks from germanium (Ge^+ , Ge^{2+}). Apart from these predominantly single-atom ions, small (i.e. few-atom) cluster ions, characteristic for evaporation of chalcogenide materials [28], can also be identified (Fig. 1). The formation of somewhat larger clusters may be enhanced, because the sample temperature (80 K) in the present work is higher than the more usual ~ 30 K in LEAPT experiments [29]. As the temperature was lowered the samples became more brittle, and they all fractured upon application of the voltage below 60 K.

In LEAPT, clusters originate from complex ionization and evaporation processes that are difficult to quantify; the presence of clusters cannot be directly translated into structural conditions within the sample. The high background noise in the mass spectrum (Fig. 1) and the complexity of the ionization processes (correlated multiple events due to correlated field evaporation—characteristic of metallic samples, field-induced dissociation (ionization) of cluster ions, and possible formation of undetected neutral clusters)

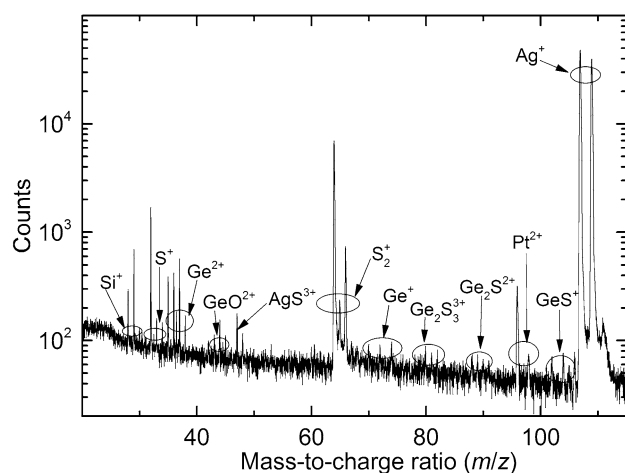


Fig. 1 Characteristic mass spectrum from thin-film $\text{Ag-Ge}_{40}\text{S}_{60}$ with the identified ionic species. The range below a mass-to-charge ratio (m/z) of 20, containing mainly silicon, is omitted from the plot. No ions were observed above $m/z = 120$

[30] preclude accurate determination of absolute composition. However, in parallel with results on Ge-Sb-Te films [31], we find that relative trends in the content of individual atomic species (Ag , S and Ge in the present case) can be revealed.

To map relative compositions, the cluster ions were registered as the corresponding individual Ag , S and Ge atoms. The resulting 2-D projected compositional maps (Fig. 2; see also Fig. S1 in supplementary material) show the microstructure of the $\text{Ag-Ge}_{40}\text{S}_{60}$ films on a nanometer length-scale. The mechanisms of growth on the silicon tips and any deposition shadowing effects remain to be studied in detail, and the microstructure is presumed to be similar to that in films deposited on flat substrates. The silicon tip itself, not shown in the figure, starts to be detected for z greater than ~ 70 nm, as seen in the curved lower edge of the projected composition maps (Fig. 2, first and second columns, i.e. parts (a), (b), (d), (e), (g), (h)). The microstructure of the subsurface, $z < 15$ nm, layer at the top may be influenced by grain growth in the Ag layer during OIDD [32]. Our main focus is on the reconstructed compositions of depths, z , between ~ 15 and ~ 70 nm. Despite the experimental difficulties, noted above, the compositional projections suggest the co-existence of regions with two distinct compositions.

Type-I regions are Ag -rich. For these, the TOF mass signal is dominated by Ag^+ ions and little can be deduced about the Ge-S host matrix. These regions typically extend beyond the sampling volume of $\sim 40 \times 40 \times 80 \text{ nm}^3$. One of the analyzed sample tips consisted of type-I region only.

Type-II regions are relatively Ag -poor and smaller than type I, being typically 10–20 nm across. Most of the Ge-S and Ag-S cluster ions were detected from these regions (Fig. S1 in supplementary material).

The present LEAPT observations of two compositionally distinct types of region have some similarities to the μm -scale interpretations of Ag -poor regions embedded within a continuous Ag-As-S matrix [24, 25]. Within the detection limit the present LEAPT study does not provide any clear evidence for nanocrystals that have been seen in other studies of photodoped films [18, 19].

For the Ag -doped thin-film $\text{Ge}_{40}\text{S}_{60}$, 3-D image reconstruction, Fig. 3, shows that within a Ag -rich Type-I region the microstructure has features, ~ 5 nm wide (highlighted with the ellipses in Fig. 3a). These features, which we describe as nanocolumns, have somewhat higher Ag content than the rest of the region. Unlike in Fig. 2, the reconstruction is based only on monatomic ions of Ag , S and Ge directly detected in the mass spectrum (Fig. 1). Only 10% of all the detected Ag^+ ions are plotted in Fig. 3a.

In the standard view of OIDD, it is considered to occur by migration of a stable diffusion front, a process that would not generate lateral non-uniformity. But there is

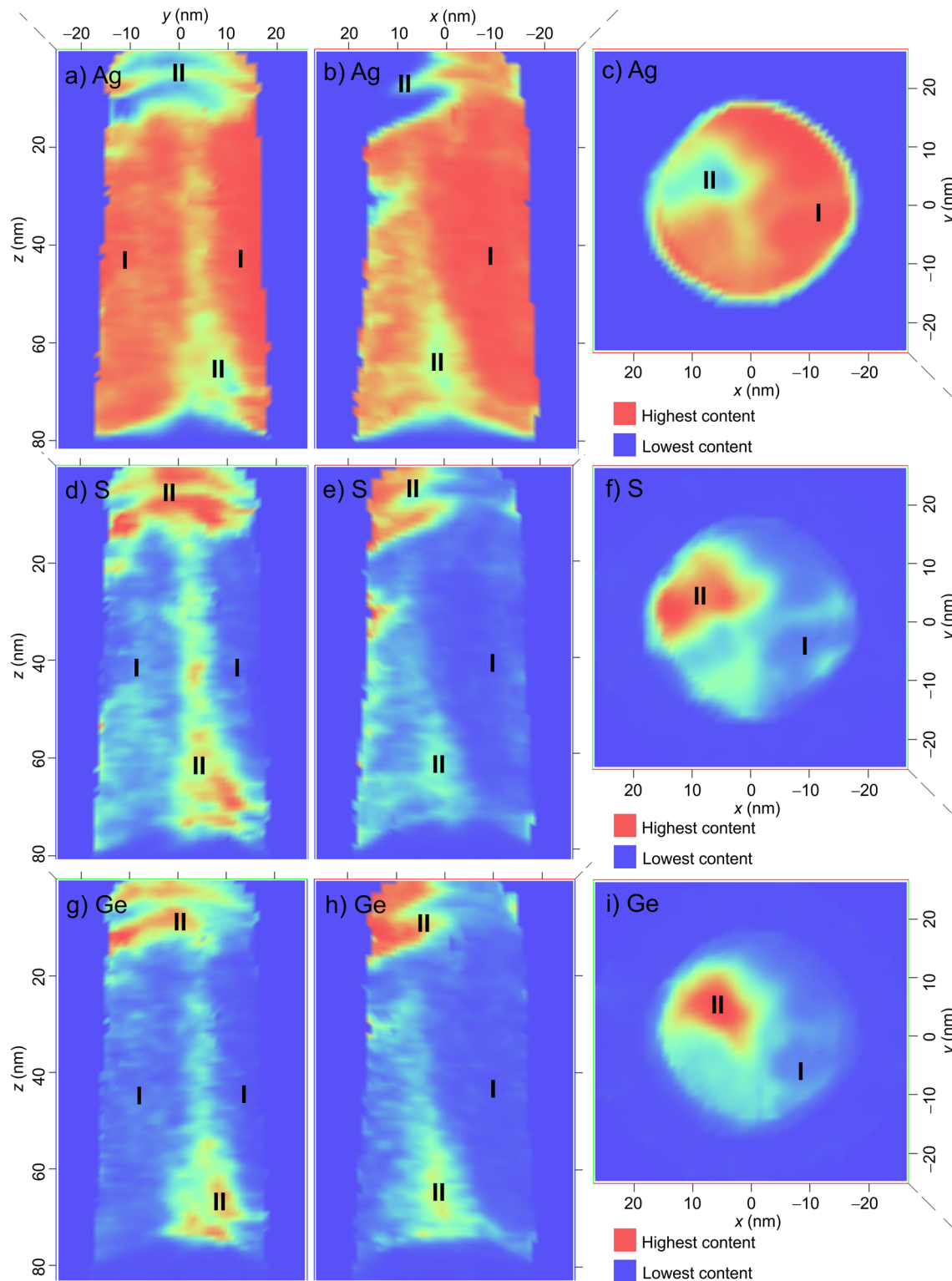


Fig. 2 LEAPT projections of relative compositional maps of the individual atomic species: **a–c** Ag, **d–f** S and **g–i** Ge viewed in different plane projections. The labels *I* and *II* refer to Ag-rich and Ag-poor regions, respectively. The red color represents the relative maximum and the blue color the relative minimum content for the given elements. As noted in the text, only qualitative trends within one element can be reproduced. The color indicates a relative scaling fac-

tor for each individual atom; the same color, compared among all the elements, does not correspond to the same atomic percentage. The compositional non-uniformity in $z=15\text{--}70$ nm, seen in parts **a**, **b**, **d**, **e**, **g** and **h**, is of interest. The subsurface layer up to ~ 15 nm in depth may be influenced by grain growth in the top layer Ag during OIDD, while the curved lower edge, at $z > 70$ nm is because of the silicon tip, radius of curvature < 50 nm. (Color figure online)

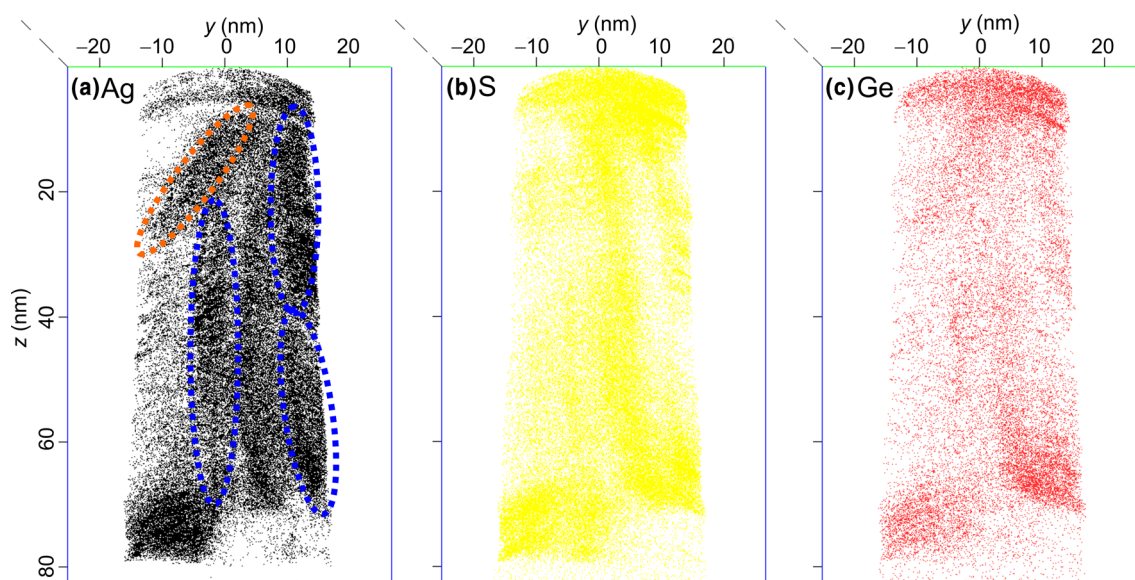


Fig. 3 A 3-D representation of the individual elements **a** Ag, **b** S and **c** Ge. Only 10% of the total detected Ag content is shown. The *blue* and *orange ellipses* highlight the oriented nanocolumns with excess

Ag that exist inside type-I regions (Fig. 2). The main focus is on the distribution of the elements at depths, *z*, from ~15 to ~70 nm. (Color figure online)

evidence that there can be compositional non-uniformity developing in the early stages of OIDD in thin-film Ge–S [16]. The neutron reflectance measurements assume vertical non-uniformity only [16]; optical modeling of lateral uniformity is challenging, but this does not preclude lateral non-uniformity. It therefore seems that the microstructure may have its origins in the as-deposited film prior to OIDD. In general, thermally evaporated films, deposited onto substrates at ~300 K, can have a low-porosity structure with clearly defined columns (a few tens of nm in diameter) parallel to the growth direction [33, 34]. In the present work, the columnar structure has a characteristic period (column diameter) of roughly 5 nm. Interestingly, this is similar to the resolution limit found in photolithography of Ag-photodoped thin-film Ge–Se [35].

If the a-Ch has a columnar microstructure, then that must influence the progress of OIDD. The outcome is complicated because the microstructure is also likely to evolve during OIDD. For example, the Ag-photodissolution rate is lower in thin-film $\text{Ge}_{30}\text{S}_{70}$ which has been exposed to light prior to OIDD, an effect attributed to photodensification [33, 36]. Such effects can be large in obliquely-evaporated films, in which the density of the a-Ch can be reduced by tens of percent [26, 37]; for example, photodensification of up to 27% has been found for obliquely-deposited thin-film $\text{Ge}_{25}\text{S}_{75}$ [38].

Despite such possible rearrangements, the aligned nanocolumns, seen in Fig. 3a, are most likely related to a similar columnar structure in the as-deposited film before OIDD. The pattern highlighted by the orange ellipse in Fig. 3a, and

the presence of Type-II regions, show that the microstructure is, however, not completely ordered and aligned, but shows some non-uniformity, whether governed by the film growth or by possible later rearrangements.

Using X-ray absorption spectroscopy, Souchier et al. [39] detected different local environments of Ag atoms in Ge–S doped by electroformation, a process which may result in locally distributed Ag-doped regions [3], therefore being sensitive to a host-matrix microstructure. The fraction of metallic-like bonding of Ag increased from <15 to 30–40% after an external voltage was applied to switch the sample into the ON state. The Ag-rich Type-I regions (Fig. 2) in the present work may be related to the metallic component observed in the samples of Souchier et al. before switching. Correspondingly, the Type-II regions in the present work may be related to the component of non-metallic bonding detected by Souchier et al. [39], and could correspond to the a-Ag–Ge–S matrix containing more of units such as Ge–AgS_3 and Ge–GeS_3 [40]. By analogy with the work of Souchier et al., a possible origin of the Type-I and Type-II regions is non-uniformity in the supply of Ag.

Stehlik et al. [41] calculated, from impedance spectroscopy measurements, that the concentration of free Ag^+ ions, 10^{21} – 10^{22} cm^{-3} , is almost independent of Ag content, while the diffusion coefficient increases by four orders of magnitude with increasing doping level in ternary Ag–As–S bulk glasses. The apparent ionic transfer number increases with silver [42, 43], but its relation to the structural environment in the electrolyte is still not fully understood. The almost constant high concentration and high

mobility of free Ag^+ ions in the doped glass [41], may in the light of the present LEAPT study suggest an important role of the thin-film microstructure on CF growth/dissolution. The type-I regions, Ag-rich, containing aligned metallic-like nanocolumns, with excess Ag, are the likely preferred locations for filament formation.

4 Conclusions

The present LEAPT study shows the microstructural complexity of Ag-photodoped thin-film chalcogenides and reveals two distinct compositions: Ag-rich Type-I regions, and Ag-poor Type-II regions. Although the columnar structure of the as-deposited film may evolve during OIDD, it appears to be at least partially preserved, and it manifests itself in the aligned nanocolumns, ~5 nm wide, within the Type-I regions. These nanocolumns, being somewhat Ag-rich compared to the Type-I regions in which they are embedded, may be the preferred locations for the growth of conducting filaments when a voltage is applied to PMC.

Acknowledgements JO, MC and ALG acknowledge financial support by the World Premier International Research Center Initiative (WPI), MEXT, Japan. TW acknowledges the MEYS CR project KONTAKT II (CR-USA) LH14059 for financial support.

Funding The funding was provided by Ministerstvo Školství, Mládeže a Tělovýchovy (Grant No. LH14059) and Ministry of Education, Culture, Sports, Science, and Technology.

Open Access This article is distributed under the terms of the Creative Commons Attribution 4.0 International License (<http://creativecommons.org/licenses/by/4.0/>), which permits unrestricted use, distribution, and reproduction in any medium, provided you give appropriate credit to the original author(s) and the source, provide a link to the Creative Commons license, and indicate if changes were made.

References

1. R. Waser, M. Aono, *Nat. Mater.* **6**, 833 (2007)
2. A.H. Edwards, H.J. Barnaby, K.A. Campbell, M.N. Kozicki, W. Liu, M. Marinella, *Proc. IEEE*. **103**, 1004 (2015)
3. M.N. Kozicki, H.J. Barnaby, *Semicond. Sci. Technol.* **31**, 113001 (2016)
4. M.N. Kozicki, M. Mitkova, *J. Non-Cryst. Solids* **353**, 567 (2006)
5. B.J. Eggleton, B. Luther-Davies, K. Richardson, *Nat. Photon.* **5**, 141 (2011)
6. J. Orava, T. Wagner, M. Krbal, T. Kohoutek, M. Vlcek, P. Klápetek, M. Frumar, *J. Non-Cryst. Solids* **354**, 533 (2008)
7. J.M. Conde Garrido, F. Macoretta, M.A. Urena, B. Arcondo, *J. Non-Cryst. Solids* **355**, 2079 (2009)
8. J. Orava, M.N. Kozicki, S.N. Yannopoulos, A.L. Greer, *AIP Adv.* **5**, 077134 (2015)
9. R. Symanczyk, R. Dittrich, J. Keller, M. Kund, G. Muller, B. Ruf, P.-H. Albarede, S. Bournat, L. Bouteille, A. Duch, *IEEE 8th Non-Volatile Memory Technology Symposium* (2007). doi:10.1109/NVMT.2007.4389950
10. I. Valov, R. Waser, J.R. Jameson, M.N. Kozicki, *Nanotechnology* **22**, 254003 (2011)
11. I. Valov, M.N. Kozicki, *J. Phys. D* **46**, 074005 (2013)
12. T. Wagner, M. Frumar, in *Photo-Induced Metastability in Amorphous Semiconductors*, ed. by A.V. Kolobov (Wiley-VCH GmbH & Co. KGaA, Weinheim, 2003), pp. 160–181
13. H. Jain, M. Vlcek, *J. Non-Cryst. Solids* **354**, 1401 (2008)
14. T. Wagner, A. Mackova, V. Perina, E. Rauhala, A. Seppala, S.O. Kasap, M. Frumar, *J. Non-Cryst. Solids* **299–302**, 1028 (2002)
15. J. Orava, T. Kohoutek, T. Wagner, Z. Cerna, M. Vlcek, L. Benes, B. Frumarova, M. Frumar, *J. Non-Cryst. Solids* **355**, 1951 (2009)
16. Y. Sakaguchi, H. Asaoka, Y. Uozumi, Y. Kawakita, T. Ito, M. Kubota, D. Yamazaki, Y. Soyama, M. Ailavajhala, M.R. Latif, M. Mitkova, *Can. J. Phys.* **92**, 654 (2014)
17. T. Kawaguchi, S. Maruno, S.R. Elliott, *J. Appl. Phys.* **79**, 9096 (1996)
18. M.N. Kozicki, M. Mitkova, J. Zhu, M. Park, *Microelectron. Eng.* **63**, 155 (2002)
19. M. Mitkova, M.N. Kozicki, *J. Phys. Chem. Solids* **68**, 866 (2007)
20. S. Menzel, S. Tappertzhofen, R. Waser, I. Valov, *Phys. Chem. Chem. Phys.* **15**, 6945 (2013)
21. J. van den Hurk, S. Menzel, R. Waser, I. Valov, *J. Phys. Chem. C* **119**, 18678 (2015)
22. S. Ambrogio, S. Balatti, S. Choi, D. Ielmini, *Adv. Mater.* **26**, 3885 (2014)
23. K. Wolf, M.S. Ailavajhala, D.A. Tenne, H. Barnaby, M.N. Kozicki, M. Mitkova, *Emerg. Mater. Res.* **5**, 126 (2016)
24. S. Stehlik, J. Kolar, M. Frumar, T. Wagner, H. Haneda, I. Sakaguchi, *Int. J. Appl. Glass. Sci.* **2**, 301 (2011)
25. F. Kyriazis, A. Chrissanthopoulos, V. Dracopoulos, M. Krbal, T. Wagner, M. Frumar, S.N. Yannopoulos, *J. Non-Cryst. Solids* **355**, 2010 (2009)
26. J. Orava, T. Kohoutek, T. Wagner, in *Chalcogenide Glasses, Preparation, Properties and Applications*, ed. by J.L. Adam, X. Zhang (Woodhead, Cambridge, 2014), pp. 265–309
27. E. Bychkov, V. Tsegelnik, Y. Vlasov, A. Pradel, M. Ribes, *J. Non-Cryst. Solids* **208**, 1 (1996)
28. M. Frumar, B. Frumarova, T. Wagner, P. Nemec, in *Photo-Induced Metastability in Amorphous Semiconductors*, ed. by A.V. Kolobov (Wiley GmbH & Co. KGaA, Weinheim, 2003), pp. 23–44
29. F. Tang, M.P. Moody, T.L. Martin, P.A.J. Bagot, M.J. Kappers, R.A. Oliver, *Microsc. Microanal.* **21**, 544 (2015)
30. M. Muller, D.W. Saxey, G.D.W. Smith, B. Gault, *Ultramicroscopy* **111**, 487 (2011)
31. K. Hwang, J. Bae, K. Park, S. Jeon, D. Jang, C. Park, J. Ahn, S. Kim, H. Jeong, S. Nam, G. Jeong, H. Cho, *Microsc. Microanal.* **18**, 1796 (2012)
32. R. Wang, J.H. Horton, *Phys. Chem. Chem. Phys.* **5**, 4335 (2003)
33. S. Maruno, S. Ban, *Jpn. J. Appl. Phys.* **19**, 97 (1980)
34. R.J. Martin-Palma, V. Torres-Costa, C.G. Pantano, *J. Phys. D* **42**, 055109 (2009)
35. B. Block, A.O. Thornton, J. Ingwersen, W. Daschner, *US Patent No. 6033766* (2000)
36. A.V. Kolobov, S.R. Elliott, *Adv. Phys.* **40**, 625 (1991)
37. M. Takahashi, H. Onishi, O. Tada, *J. Appl. Phys.* **42**, 833 (1971)
38. K.L. Chopra, K. Solomon Harshvardhan, S. Rajagopalan, L.K. Malhotra, *Solid State Commun.* **40**, 387 (1981)
39. E. Souchier, F. D'Acapito, P. Noe, P. Blaies, M. Bernard, V. Jousseaume, *Phys. Chem. Chem. Phys.* **17**, 23931 (2015)
40. J. Akola, B. Beuneu, R.O. Jones, P. Jovari, I. Kaban, J. Kolar, I. Voleska, T. Wagner, *J. Phys.* **27**, 485304 (2015)
41. S. Stehlik, K. Shimakawa, T. Wagner, M. Frumar, *J. Phys. D* **45**, 205304 (2012)
42. M. Kawasaki, J. Kawamura, Y. Nakamura, M. Aniya, *Solid State Ion.* **123**, 259 (1999)
43. E. Bychkov, *Solid State Ion.* **180**, 510 (2009)